Imaging iron ore from the Quadrilátero Ferrífero (Brazil) using geophysical inversion and drill hole data

Dionísio U. Carlos [a,b,*], Leonardo Uieda [a], Valeria C.F. Barbosa [a]

[a] Observatório Nacional, Departamento de Geofísica, Gal. José Cristino, 77, Rio de Janeiro, RJ 20921-400, Brazil
[b] Vale, Departamento de Exploração de Ferrosos, Avenida de Ligação, 3580, Nova Lima, MG 34000-000, Brazil

ARTICLE INFO

ABSTRACT

The Quadrilátero Ferrífero in southeastern Brazil hosts one of the largest concentrations of lateritic iron ore deposits in the world. Our study area is over the southern flank of the Gandarela syncline which is one of the regional synclines of the Quadrilátero Ferrífero. The Gandarela syncline is considered the Brazilian megastructure with the highest perspectives for iron ore exploration. Most of the iron-ore deposits from the Quadrilátero Ferrífero are non-outcropping bodies hosted in the oxidized, metamorphosed and heterogeneously deformed banded iron formations. Therefore, the assessment of the 3D geometry of the iron-ore body is of the utmost importance for estimating reserves and production development planning. We carried out a quantitative interpretation of the iron-ore deposit of the southern flank of the Gandarela syncline using a 3D inversion of airborne gravity-gradient data to estimate the shape of the iron-ore mineralization. The retrieved body is characterized by a high-density zone associated with the northeast-elongated iron formation. The thickness and the width of the retrieved iron-ore body vary along its strike increasing southwestward. The presence of a large volume of iron ore in the southwest portion of the study area may be due to the hinge zone of the Gandarela syncline, which is the zone of maximum compression. Our estimated iron-ore mass reveals variable dip directions. In the southernmost, central and northernmost portions of the study area, the estimated iron body dips, respectively, inwards, vertically and outwards with respect to the syncline axis. Previous geological mapping indicated continuous mineralization. However, our result suggests a quasi-continuous iron-ore body. In the central part of the study area, the estimated iron-ore body is segmented into two parts. This breakup may be related to the northwest-trending faults, which are perpendicular to the northeast-trending axis of the Gandarela syncline. Our estimated iron-ore mass agrees reasonably well with the information provided from the lithologic logging data of drill holes. In this geophysical study, the estimated iron-ore reserves are approximately 3 billion tons.

© 2014 Elsevier B.V. All rights reserved.

1. Introduction

The Quadrilátero Ferrífero (QF) comprises an area of about 7000 km^2 and hosts one of the largest concentrations of lateritic iron-ore deposits in the world. The QF is located in central Minas Gerais state, southeastern region of Brazil (Dorr, 1965). The QF has a quadrangular shape due to the dome and basin structures of the Minas Supergroup (Fig. 1). Most of the iron ore in the QF are hosted in the oxidized, metamorphosed and heterogeneously deformed Banded Iron Formations (BIFs) of the Cauê Formation, the so-called itabirites. The BIFs are altered sedimentary deposits with laminated rocks formed by alternating layers of silica and hematite–magnetite, as well as carbonates and iron silicates.

In this study, we have interpreted a set of airborne gravity gradiometry data collected over the southern flank of the Gandarela syncline, which is an important known geologic feature of the QF. The Gandarela syncline is located in the north–northeast portion of QF and it extends for 32 km. Based on geologic mapping, the Gandarela syncline is a northeast–southwest-trending regional-scale reclined fold with a hinge zone dipping to the southeast. Nowadays, the Gandarela syncline is considered the Brazilian region with the highest perspectives for iron ore exploration. However, to date the 3D shape of the iron-ore deposit is unknown. We have applied a fast gravity-gradient inversion method to estimate the 3D geometry of the iron-ore deposits of the Cauê Formation over the Gandarela syncline. The inversion method estimates a voxel image of the density-contrast distribution in the subsurface, which produces the shape of the unknown body. The estimate is obtained by iteratively aggregating small right rectangular prisms with given density contrasts around prisms called "seeds" which operate as gross skeletal outlines of the geologic bodies. This growth process follows the

* Corresponding author at: Observatório Nacional, Departamento de Geofísica, Gal. José Cristino, 77, Rio de Janeiro, RJ 20921-400, Brazil. Tel.: +55 31 3215 4201; fax: +55 31 3215 4042.

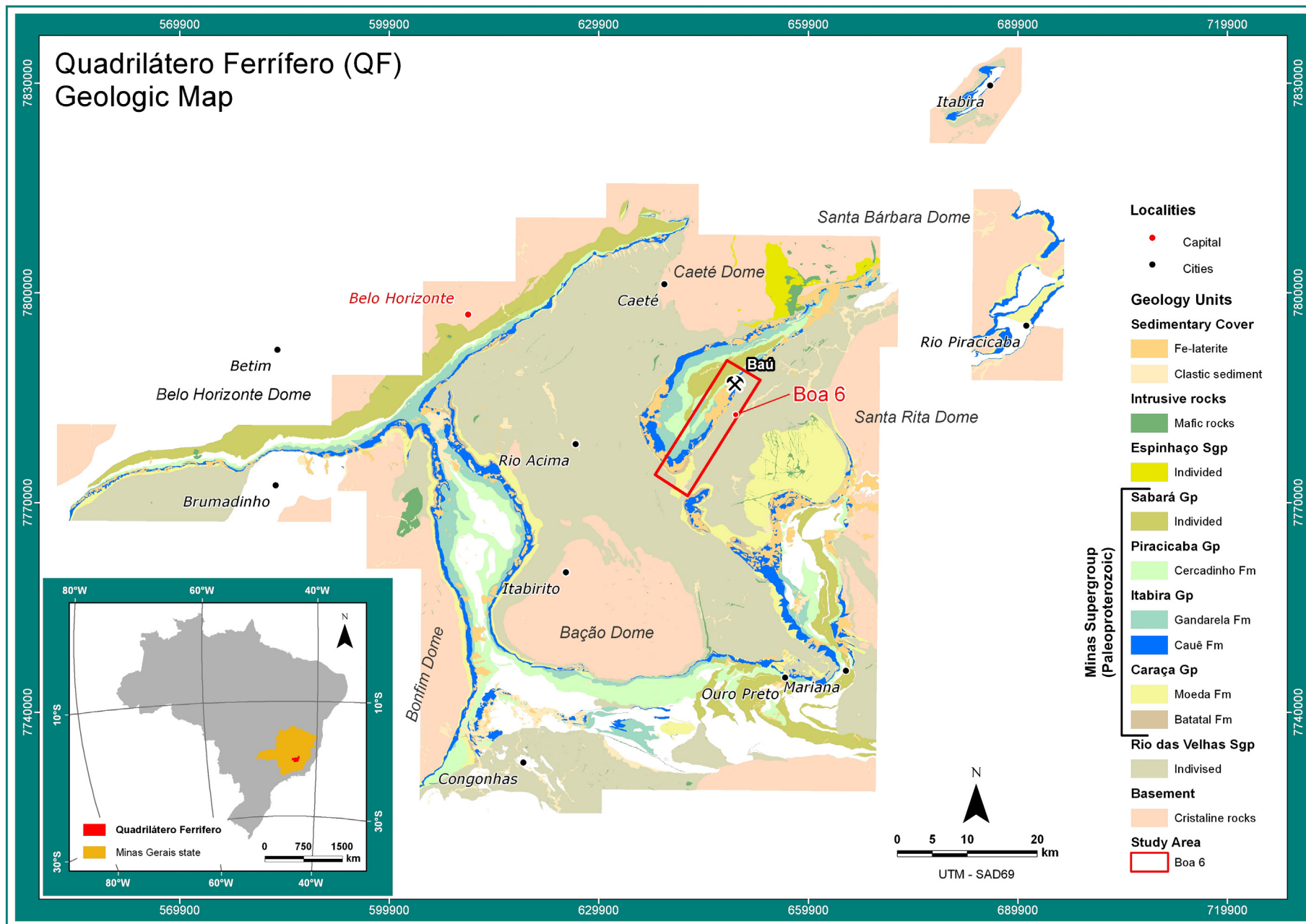*E-mail address:* dionisio.carlos@vale.com (D.U. Carlos).

Fig. 1. Regional geological map of the Quadrilátero Ferrífero area located at Minas Gerais state, Brazil. After Lobato et al. (2005). The study area named Boa 6 is outlined with a red rectangle and it is also shown as an inset in the map of Brazil. (For interpretation of the references to color in this figure legend, the reader is referred to the web version of this article.)

restrictions that the estimated bodies should be as compact as possible and that the data predicted by the estimate should fit the observed data as close as possible. The advantage of this iterative procedure is that it neither requires the full computation or storage of a sensitivity matrix nor the solution of large equation systems. Moreover, we have used borehole information to verify the degree of confidence between lithologic logging data and our estimated 3D image of the iron-ore formation.

2. Geological background

2.1. Regional geology

The Quadrilátero Ferrífero is located at the southeastern border of the São Francisco Craton, southeastern Brazil (Fig. 1). According to Alkmim and Marshak (1998) the most important lithostratigraphic units of the Quadrilátero Ferrífero are: (1) the Archean crystalline basement, (2) the Rio das Velhas Supergroup, (3) the Minas Supergroup, (4) the Post-Minas Intrusives and (5) the Itacolomi Group.

Fig. 2 shows the generalized stratigraphic column of the QF. Basement crystalline rocks include a gneiss/migmatite complex and two generations of voluminous Late Archean plutons: calk-alkaline and anorogenic granites (Alkmim and Marshak, 1998). The Rio das Velhas Supergroup consists of greenstone (basalt and komatiite), rhyolitic lava and intercalated sedimentary rocks. Sedimentary units of the Rio das Velhas Supergroup include Algoma-type banded-iron formations (BIFs), carbonates and siliciclastics. The Minas Supergroup is a metasedimentary unit that unconformably overlies the Rio das Velhas Supergroup. According to Alkmim and Marshak (1998), the Minas Supergroup strata resist erosion, forming ridges that tower above the regions which are underlain by less resistant basement or greenstone rocks. These characteristics of the Minas Supergroup shaped the geomorphology of the southern Brazil highlands giving rise to high relief in this region. Alluvial conglomerate and sandstone made up the basal units of the Minas Supergroup. These units grade upward into shallow-water marine pelites of the Tamanduá and Caraça Groups. The Lake Superior-type Cauê banded-iron Formation lies on Caraça metasediments. The Cauê Formation is a carbonate sequence of the Gandarela Formation. Lying locally unconformably on the Gandarela Formation, the Piracicaba Group comprises a thick pile of shallow-water and deltaic strata. Separated from the Piracicaba Group by an unconformity, the Sabará Group is a thick sequence of turbidites, tuffs, volcaniclastics, conglomerates and diamictites derived from a source to the east–southeast. The Post-Minas intrusives comprise thin, undated, pegmatite veins cutting Minas rock (Alkmim and Marshak, 1998; Herz, 1970). Finally, the Itacolomi Group is a unit consisting of alluvial sandstones, conglomerates and minor pelites (Dorr, 1969) deposited in intramontane grabens (Alkmim and Martins-Neto, 2012).

2.2. Local geology

The study area, named Boa 6, is located within part of the Gandarela syncline (Fig. 3). The Gandarela syncline (Dorr, 1969) is a megastructure formed in the early phases of the Transamazonian orogeny (~2.0 Ga), which affected the Quadrilátero Ferrífero. The Gandarela syncline is one of the regional synclines of the Quadrilátero Ferrífero that was probably originated from a regional extensional event (Chemale et al., 1994). The Gandarela syncline has a northeast–southwest trend and it was fractionized by Brazilian faults (~600 Ma), which also caused re-foldings, especially, in its northeast region. It is an allochthonous, overturned, northwest-verging structure, where the Minas Supergroup strata are folded around a northeast–southwest-trending axis. Chemale et al. (1994) divided the Gandarela syncline into three structural domains: (1) northeastern area, (2) central area and (3) southern area. The northeastern area of the Gandarela

syncline, with the axis trending at N60°E, is delimited by the Cambotas and Fundão Faults (Fig. 3). The central area, with the axis trending at N40°E, represents the less-deformed part of the Gandarela syncline. The southern area of the syncline has approximately a north–south-trending axis and it is interpreted as an appendix of this syncline being denominated by the Palmital Homocline (Chemale et al., 1994).

The Gandarela syncline is defined for the units of the Minas Supergroup in contact with sequences of the Rio das Velhas Supergroup and in the north portion in contact with the metamorphic complex Caeté. In the Gandarela syncline, the Moeda Formation forms the base of the Minas Supergroup, which unconformably overlies the Archean Rio das Velhas Supergroup. Over most of the Gandarela syncline the Moeda lies above the Nova Lima Group rocks where they are composed predominantly of graywackes, pylittes and thin iron formations. The Moeda rocks are composed of conglomerates and quartzites and, according to Villaça and Moura (1981), the sequence is up 350 m thick in the southern part of Gandarela syncline.

The Batatal Formation, in the top of the Caraça Group, consists mainly of phyllite. The Cauê Formation comprises a 250–300 m thick sequence of iron formations (itabirites and hematites bodies) intercalated with hematitic phyllites, dolomitic pyllites and marbles. Lying conformably on the Cauê Formation, the Gandarela Formation is composed of carbonate rocks (calcitic and dolomitic marbles) with subordinate phyllites and banded iron formation (Rosière and Rios, 2004). The target for mineral exploration is the Cauê Formation that comprises banded iron-ore formation.

The Cercadinho Formation is made up of rhythmic sequence of phyllite, quartzite and ferruginous quartzite. Finally, the Sabará Group is a metavolcanic sedimentary sequence, which comprises mica schist and chlorite schist with metagraywacke intercalations, quartzite, feldspatic quartzite, ferruginous quartzite, iron-ore formation and metaconglomerates (Lobato et al., 2005).

The Quadrilátero Ferrífero is characterized by very complex geological and tectonic evolutions. In this context, geophysical study is an important tool in understanding the deep structures of the Quadrilátero Ferrífero. In this area, the first geophysical study started in the 1970s. Gasparini et al. (1979) studied the depths of Curie temperatures computed for continental areas with normal and low heat flows and concluded that the depth-to-bottom estimate of the crustal magnetized layer may correspond to vertical compositional changes within the crust. Padilha (1982) performed 2D inversions of the magnetic anomaly from the Gandarela region for estimating the dimension of magnetic sources. By using geophysical data to study gold mineralizations, Tavares (1998) identified the mining potential of the Archean greenstone terranes in the Caeté region. Silva (1999) and Rolim (2001) studied the geophysical responses of gold deposits in greenstone Rio das Velhas.

More recently, geophysical studies have been carried out to delineate the iron deposit from the Quadrilátero Ferrífero. Uieda and Barbosa (2012a) developed a new 3D gravity-gradient inversion method for estimating the shape of an anomalous density distribution and applied it to an airborne gravity gradiometry survey from the Quadrilátero Ferrífero. Martinez et al. (2013) presented a case study of applying a different method of inversion of gravity gradiometry data from the Quadrilátero Ferrífero to estimate a 3D image of the iron-ore formation and to examine the usefulness of various gravity gradient component combinations in delineating this formation.

3. Geophysical data and their relationship to known geology

In 2005 the airborne gravity gradiometry data were acquired over the study area (Boa 6) which extends in the northeast direction with dimensions of approximately 19 × 5 km The 50 flight lines had a
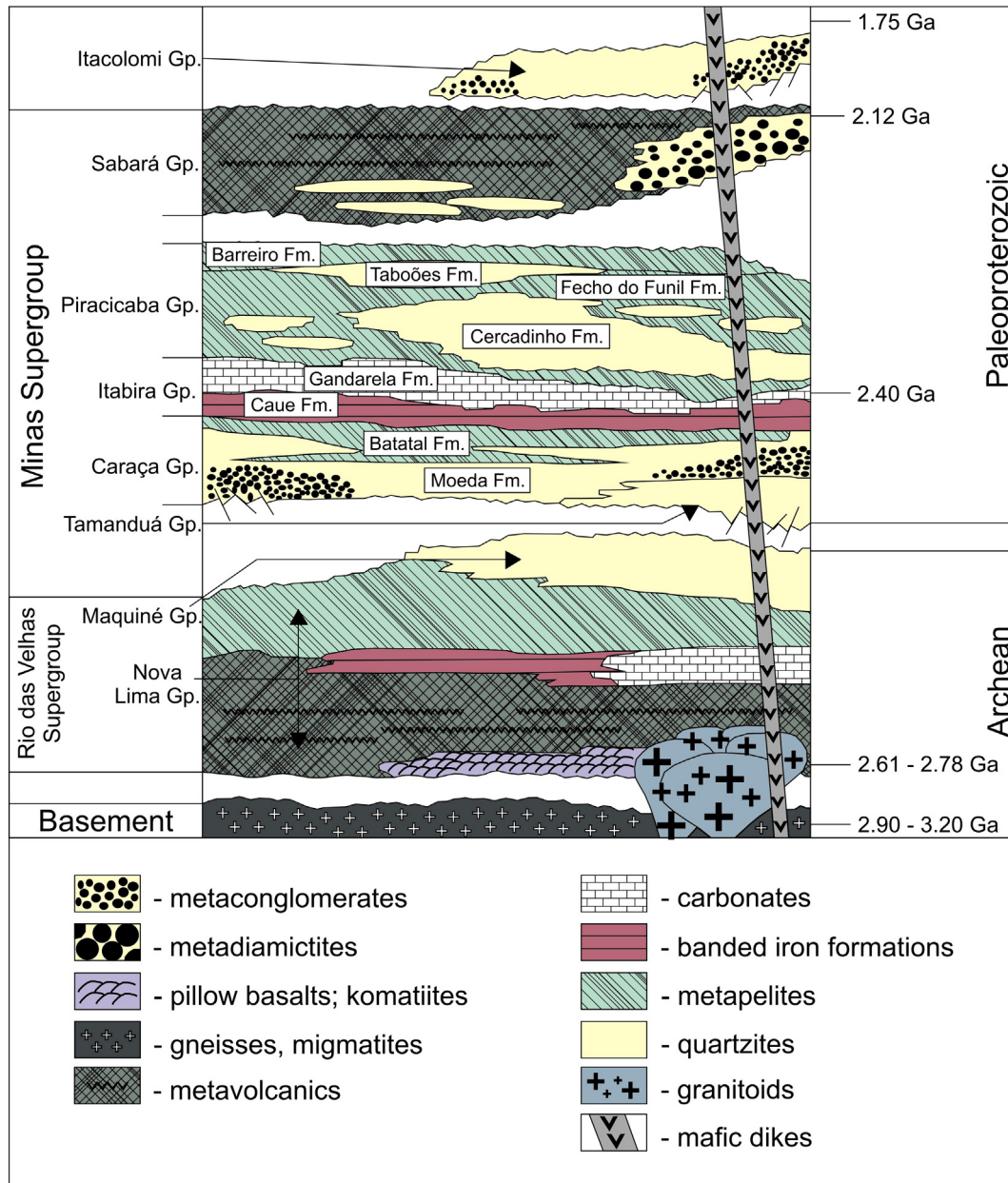
Fig. 2. Generalized stratigraphic column of the Quadrilátero Ferrífero.
After Alkmim and Marshak (1998).

northeast–southwest orientation with line spacing of 100 m. The survey was flown semi-draped at flight heights ranging from 57 to 582 m above the topographic surface.

The raw airborne gravity gradiometry data were preprocessed following these steps (Bell Geospace, 2010): (1) compensations due to the airborne survey, (2) terrain correction, (3) line corrections and (4) line leveling. The compensations due to the airborne survey include corrections for the gradients of the aircraft, of the instruments themselves and of the centripetal acceleration. The data were then corrected for the gravity gradient response produced by the rugged topography over the study area. To model this topography we approximate the space between the terrain surface and the ellipsoid by a set of vertical, rectangular, juxtaposed 3D prisms whose tops coincide with the topography surface and bases coincide with the ellipsoid. The density within each prism is assumed constant and equal to 2.36 g/cm^3. The computed gravity gradient response produced by this set of 3D prisms represents the gravity gradient response of the terrain. Hence, the terrain

correction consists of subtracting from each measured gravity gradient component the corresponding computed component of the terrain. In our terrain correction, the density of 2.36 g/cm^3 was chosen because it minimizes the covariance between the measured gravity gradiometry data and the topography. This minimization was done by using the Parasnis method (Parasnis, 1966) modified for the g_{zz}-component of the gravity gradient tensor. The third step is the line correction which calculates the tensor components from the measured data sets and removes bulk low frequency errors. The final step is the line leveling which consists of minimizing the intersection errors between survey and tie lines in a least-squares sense by adjusting the line bias levels using a methodology following the work of Huang (2008).

We adopt a right-handed Cartesian coordinate system with the x-axis pointing to north, the y-axis pointing to east, and with the z-axis pointing downward. Fig. 4 shows color-scaled maps of the six components of the gravity-gradient tensor over the study area
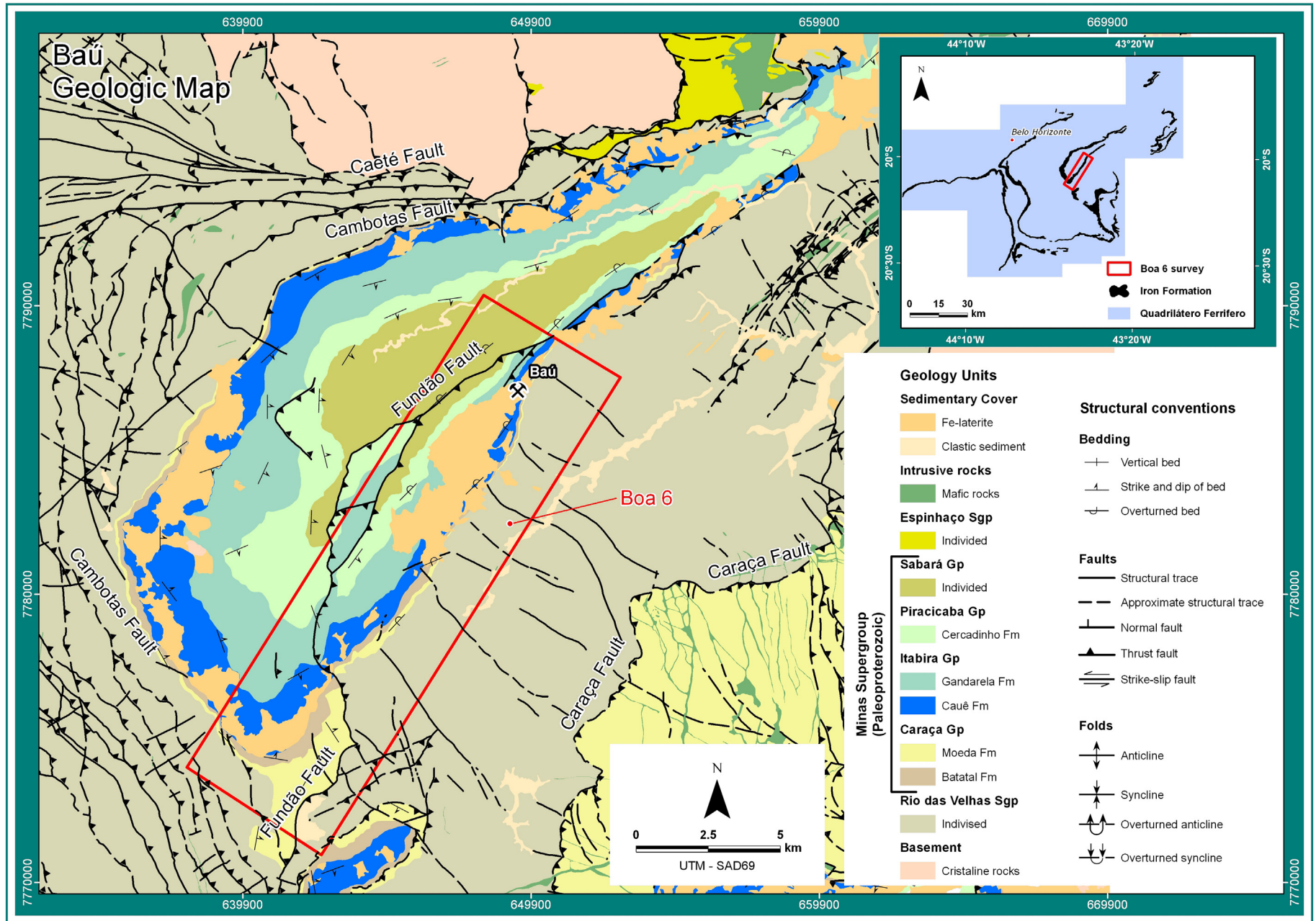
Fig. 3. Detailed geological and structural map of the Gandarela syncline area. The blue areas represent Cauê Formation (banded iron formation). The study area, named Boa 6, is outlined in red rectangle. The inset on the right shows the Quadrilátero Ferrífero area. (For interpretation of the references to color in this figure legend, the reader is referred to the web version of this article.)
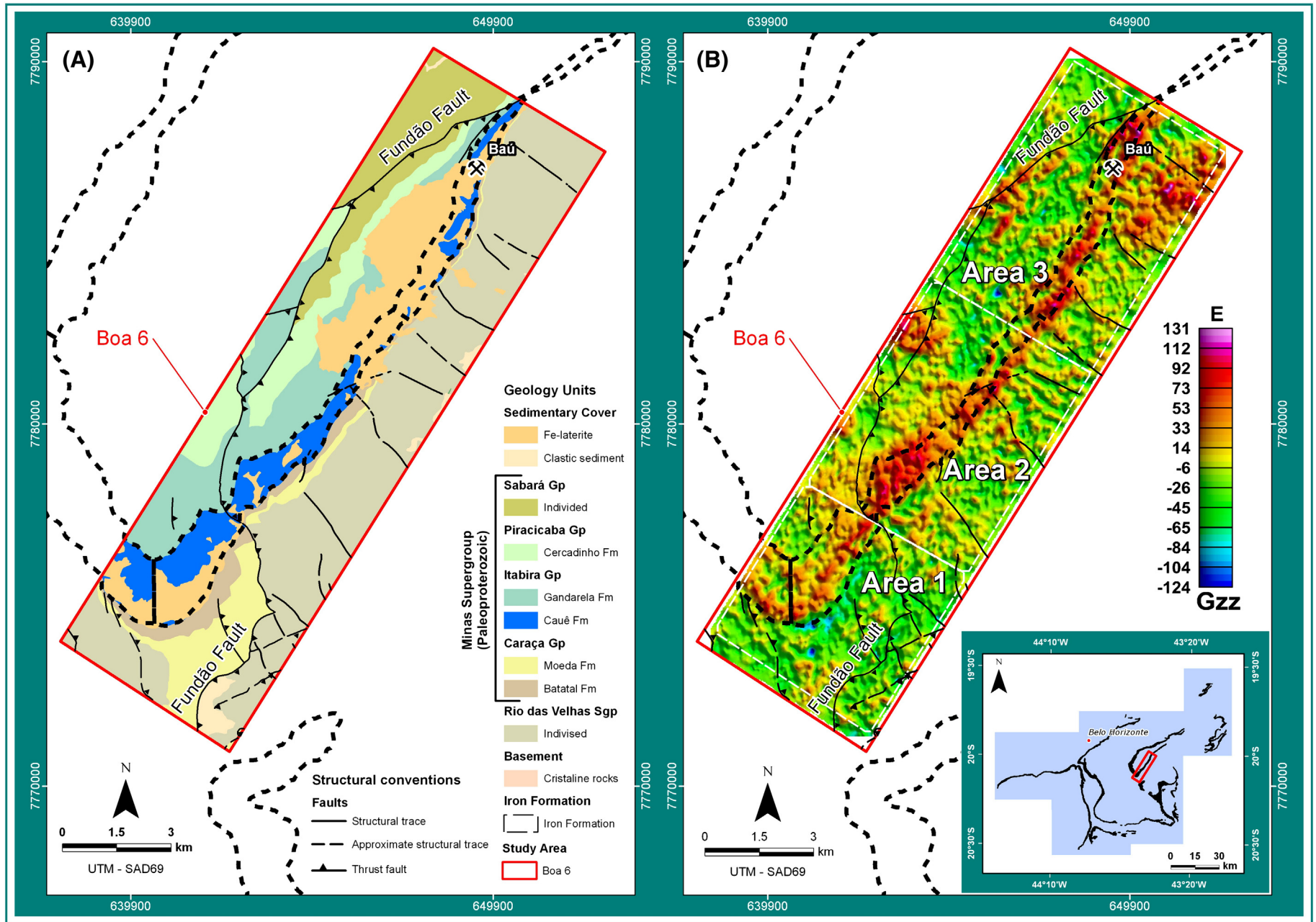After Lobato et al. (2005).
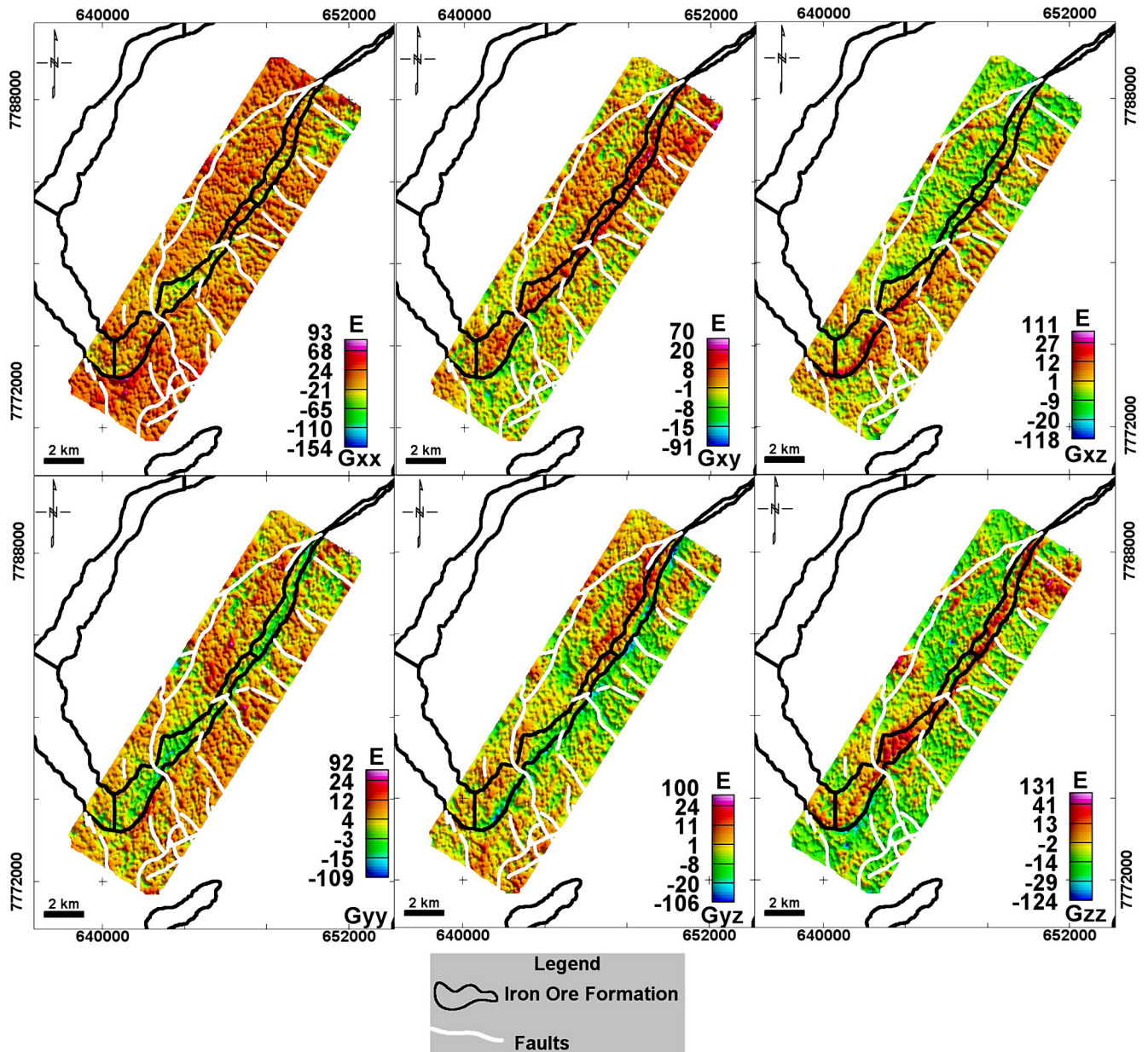
Fig. 4. Observed airborne gravity-gradient data of the study area (Boa 6 survey). The thick black lines delineate the mapped boundaries of the iron formation according to Dorr (1969). The yellow lines represent the interpreted trace of faults in the study area. (For interpretation of the references to color in this figure legend, the reader is referred to the web version of this article.)

after the preprocessing of the data. Each component of the gravity-gradient data has 15,275 measurements. There are, therefore, 91,650 observations in the study area. The unit of measure for the gravity gradient is the Eötvös (E), named for Loránd Eötvös, where 1 E is equal to 0.1 mGal·km^{-1} (or 10^{-9} s^{-2}). By comparing the detailed geologic map over the study area (Fig. 5A) with the color-scaled map of the g$_{zz}$-component of the gravity gradient tensor, we can see that the highest values of the g$_{zz}$-component match the iron-ore deposit of the Cauê Formation. Visual inspection of the data also allows delineating the lateral boundaries of the iron-ore body which agree with the geologic mapping accomplished by Dorr (1969) shown in Fig. 5B by the dotted black line. However, this visual inspection raises the following questions: 1) Is the iron-ore body a continuous or a segmented source? 2) Do the faults in the study area control the shape of the iron-ore body? 3) Does the iron-ore body have constant or variable thickness? 4) Does the iron-ore body have a constant dip? 5) Does the Gandarela syncline control the shape of the iron-ore body?

The drilling database in the study area contains 151 boreholes with variable footage. In this study area, the drill program has been carried out during the early stage of the mineral exploration project and before the geophysical surveys. With an average drilling footage of 200 m, most boreholes reached the banded iron-ore formation of the Cauê Formation which is considered the main targeted rock in the Quadrilátero Ferrífero. In general, the lithologic logging data of the boreholes indicated a shallow-seated iron-ore deposit. Table 1 summarizes the average densities of the most important lithologies drilled in this study area.

4. Methodology

Our work aims at estimating the 3D geometry of the iron-ore body from the Quadrilátero Ferrífero. To do this, we apply the robust 3D gravity-gradient inversion developed by Uieda and Barbosa (2012a), and later improved upon by Uieda and Barbosa (2012c), to jointly invert

Fig. 5. (A) Geologic map of the study area. (B) g$_{zz}$-component of the gravity gradient tensor showing Areas 1–3 which were used by applying Uieda and Barbosa's (2012a) method. The dotted black lines delineate the mapped boundaries of the iron formation according to Dorr (1969). The Quadrilátero Ferrífero area is shown as inset in (B).

Table 1
The main lithological types founded in the survey area.
After Braga (2009).

Lithology	Density (g/cm³)	Description
Duricrust (Canga)	3.20	Near-surface lithology which overlies the iron-ore formation. Its thickness varies from a few centimeters to about a few meters (~30 m). The duricrust consists of high concentrations of iron oxides and iron hydroxides with high contents of iron (about 58%), phosphorus and aluminum.
Friable hematite	3.10	With an approximately lenticular shape, the thickness of the friable hematite ranges from a few meters to tens of meters and its composition is 65% of the iron being rich in specular hematite (specularite).
Hard hematite	4.70	Displaying a massive or foliated structure, the thickness of the hard hematite ranges from a few meters to about 50 m and its composition is 67% of the iron.
Goethitic hematite	3.10	Friable lithology which is composed of hydrated hematite with high concentration of goethite, usually associated with goethitic itabirites. The goethitic hematite consists of about 64% of iron being rich in phosphorus content.
Goethitic itabirite	2.60	Friable lithology which is composed of hydrated itabirite with high concentration of goethite. Its thickness varies from meters to more than 100 m. The goethitic itabirite consists of about 52% of iron with high content of phosphorus and aluminum.
Friable itabirite	2.70	Composed of specular hematite (specularite) and quartz, the friable itabirite has a low iron content of about 47%.
Hard itabirite	3.11	Composed of a low iron content of about 40%, the hard itabirite is usually found with friable itabirite.

multi-component gravity gradiometer data. The inversion method estimates the geometry of an anomalous density distribution represented by a mesh of homogeneous right-rectangular prisms with known density-contrasts. This is accomplished not by means of least-squares estimation, as in the more traditional inversions, but rather through an iterative algorithm that builds the solution one prism at a time. The first step in such algorithm is to define the dimensions of the prism mesh, such as its total extent and number of prisms. Next, the user is required to specify "seed" prisms by choosing their location in the mesh and giving them density values. The algorithm then begins to grow the solution by the successive aggregation of new prisms around the seed prisms. When a new prism is added, it receives the density value of the seed to which it was aggregated. The choice of the new prisms for aggregation is not done randomly. Only prisms in the immediate vicinity of the solution are available for aggregation and the search for new prisms is done systematically. At each iteration, the prism chosen to be incorporated is one whose addition reduces the data misfit and keeps the solution as compact as possible. Thus, this growth algorithm expands the initial seeds to produce an estimated geometry of the density distribution. For better understanding, Uieda and Barbosa (2012b) provide an animation of the growth process during the inversion of synthetic g_{zz}-component data. It is important to note that each seed can have a different density value. Thus, the method of Uieda and Barbosa (2012a) can be used to invert for multiple bodies with varying densities. Another important feature of this method is that there are no large sensitivity matrices or equation systems involved. Hence, it is a fast and memory efficient method, able to invert large datasets using fine prism meshes. The above-mentioned characteristics of Uieda and Barbosa's (2012a) method make it ideal for estimating the 3D geometry of the iron-ore body from the Quadrilátero Ferrífero.

The cornerstone of Uieda and Barbosa's (2012a) method is the choice of the seeds (their locations and density contrasts). The chosen seeds operate effectively as gross skeletal outlines of the geologic bodies. In our work, the horizontal locations of the seeds were chosen based on the positive and elongated northeast–southwest anomalies of the g_{zz}-component of the gravity-gradient data (Fig. 5B). The seeds were placed at the depths of 50 m based on the overall information from the boreholes that the iron-ore deposit is near the surface and no deeper than 350 m.

4.1. Inversion strategies

The study area contains a total of 91,650 gravity-gradient observations. Our goal is to produce a detailed view of the 3D geometry of the iron-ore body by jointly inverting the preprocessed data of the six components of the gravity-gradient tensor (Fig. 4) using the method of Uieda and Barbosa (2012a). As pointed out before, in this inversion method the earth model comprises a mesh of right-rectangular prisms

that follows the topography of the study area and encloses the targeted bodies. This kind of earth model produces a voxel image of the density-contrast distribution in the subsurface. The smaller the prisms, the finer the discretization of the subsurface. Hence, a fine mesh of prisms is required for the representation of arbitrarily complex density-contrast distributions. Because we want to estimate the detailed geometry of the iron-ore bodies, we discretized the subsurface region along the x-, y-, and z-directions into a fine mesh of cubes with side lengths of 30 m. Thus, the total number of prisms beneath the topography surface is about 8.5 million. To make an inversion of this size more tractable, we divided the study area into three areas named Areas 1–3 whose locations are shown in Fig. 5B.

Area 1 is located in the southernmost portion of the study area and its dimensions are 4 km in the northwest by 5 km in the northeast. Areas 2 and 3 are located in the central and northernmost portions of the study area, respectively. These areas have dimensions of approximately 7 km in the northwest by 5 km in the northeast. We chose the dimensions of these three areas based on our geological knowledge about the boundaries of the outcropping iron formations (Fig. 5A). For all three areas, the targeted rocks, like itabirite and hematite, were considered to have an average density of 3.11 g/cm³. All nontargeted rocks were considered to have a density of 2.36 g/cm³. This implies that the density contrast of the iron-ore body with the main host rocks is 0.75 g/cm³. This density-contrast value was assigned to all seeds used in the inversion.

We used the inversion method to estimate the geometry and extent of the iron-ore deposits of the Cauê Formation in each area. We preformed joint inversions by using all of the preprocessed g_{xx}-, g_{xy}-, g_{xz}-, g_{yy}-, g_{yz}- and g_{zz}-components over each area. In all inversions, we selected a mesh under the horizontal extent of the data belonging to each area whose top coincides with the topography. For these three areas the topography surface used was provided by LIDAR (Light Detection and Ranging) with 1 meter resolution.

4.2. Inversion variables of each area

In each area (Areas 1–3) the inversion was performed on a set of g_{xx}-, g_{xy}-, g_{xz}-, g_{yy}-, g_{yz}- and g_{zz}-components of gravity-gradient tensor of the corresponding area. Figs. 6–8 (panels A–C and G–I) show the six observed components of the gravity-gradient tensor over Areas 1–3, respectively. Area 1 contains 3975 observations of each of the six components (totaling 23,850 measurements), Area 2 contains 5288 observations (totaling 31,728 measurements) and Area 3 contains 5,710 observations (totaling 34,260 measurements). The subsurface region under the Area 1 was discretized along the x-, y-, and z-directions into a 225 × 227 × 52 mesh of cubes resulting in a total of 2,655,900 prisms. The discretizations of the subsurfaces under Areas 2 and 3 consist of, respectively, a 264 × 257 × 43 mesh of cubes
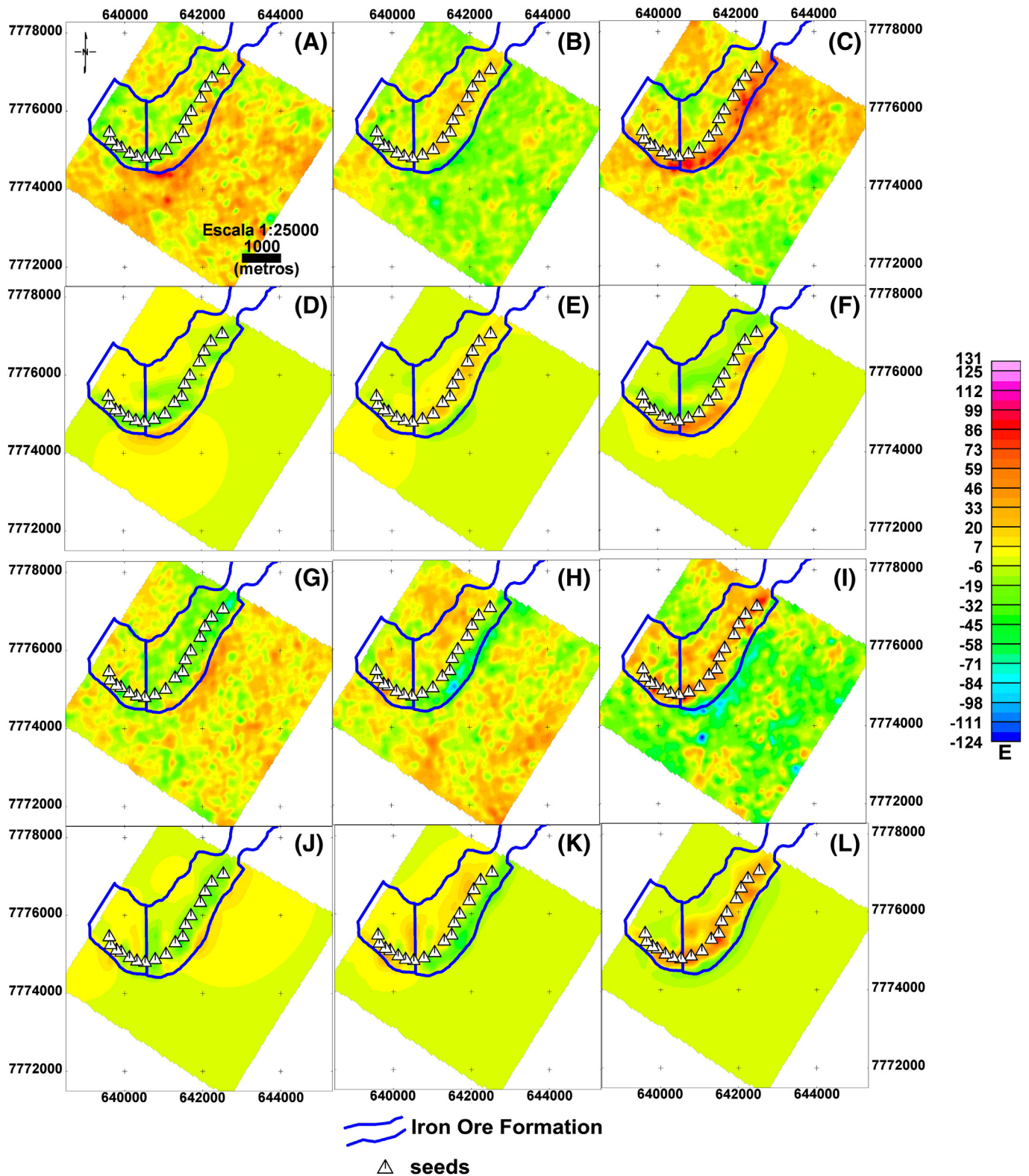
Fig. 6. Area 1. The observed (A–C and G–I panels) and predicted (D–F and J–L panels) g_{xx}-, g_{xy}-, g_{xz}-, g_{yy}-, g_{yz}- and g_{zz}-components of the gravity gradient tensor. The latter were produced by the estimated density-contrast distribution shown in Fig. 9A. The white triangles represent the horizontal coordinates of the seeds used in the inversion. The blue lines delineate the mapped boundaries of the iron formation according to Dorr (1969). The location of the Area 1 is shown in Fig. 5B. (For interpretation of the references to color in this figure legend, the reader is referred to the web version of this article.)

(totaling 2,917,464 prisms) and a 281 × 258 × 41 mesh of cubes (totaling 2,972,418 prisms). To apply Uieda and Barbosa's (2012a) method, we used a set of seeds. The number of seeds used in the inversion of both Areas 1 and 2 was 16 and of Area 3 was 21. The horizontal projections of the seeds locations are shown by white triangles in Figs. 6–8.
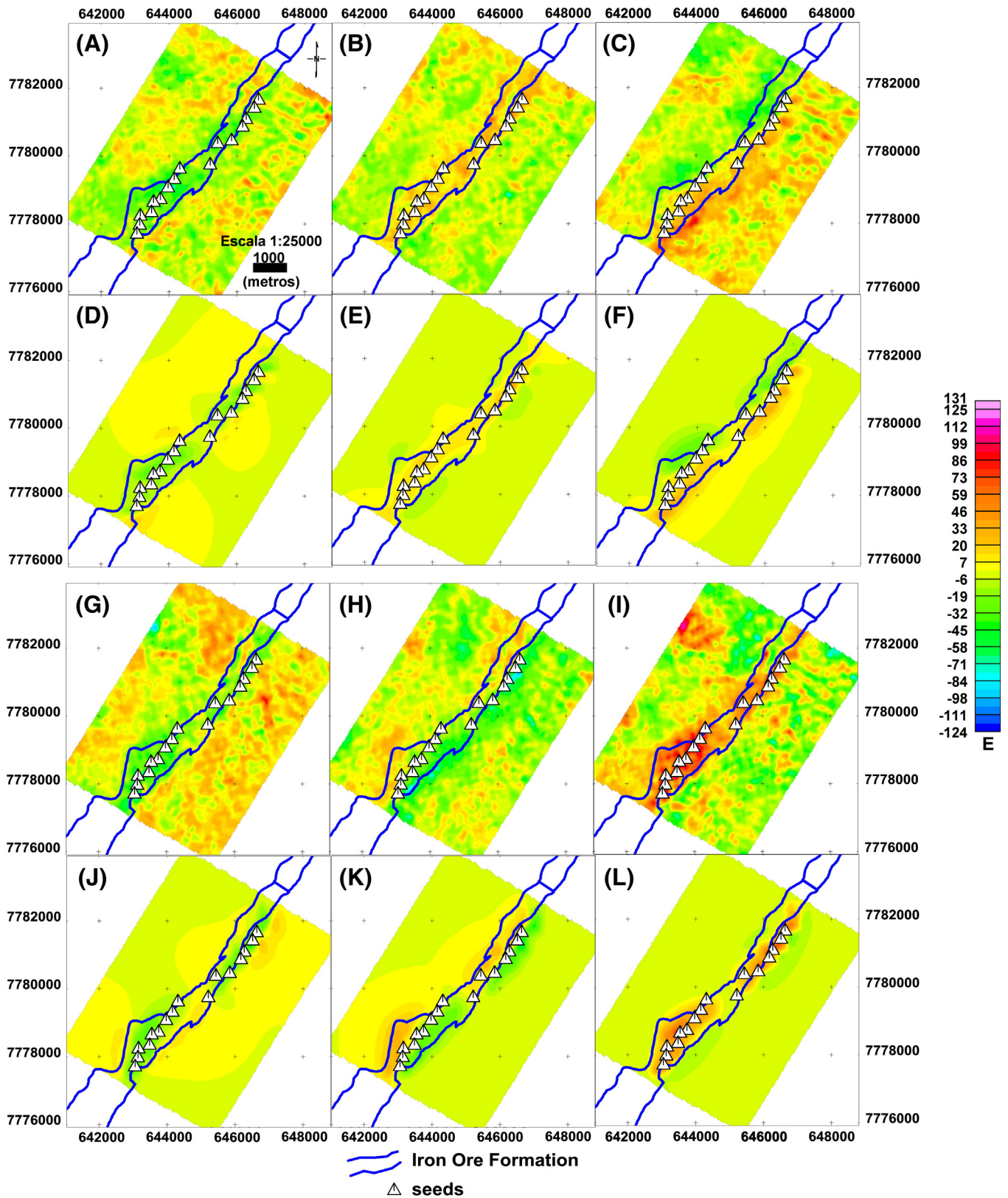
Fig. 7. Area 2. The observed (A–C and G–I panels) and predicted (D–F and J–L panels) g_{xx}-, g_{xy}-, g_{xz}-, g_{yy}, g_{yz}- and g_{zz}-components of the gravity gradient tensor. The latter were produced by the estimated density-contrast distribution shown in Fig. 9A. The white triangles represent the horizontal coordinates of the seeds used in the inversion. The blue lines delineate the mapped boundaries of the iron formation according to Dorr (1969). The location of Area 2 is shown in Fig. 5B. (For interpretation of the references to color in this figure legend, the reader is referred to the web version of this article.)
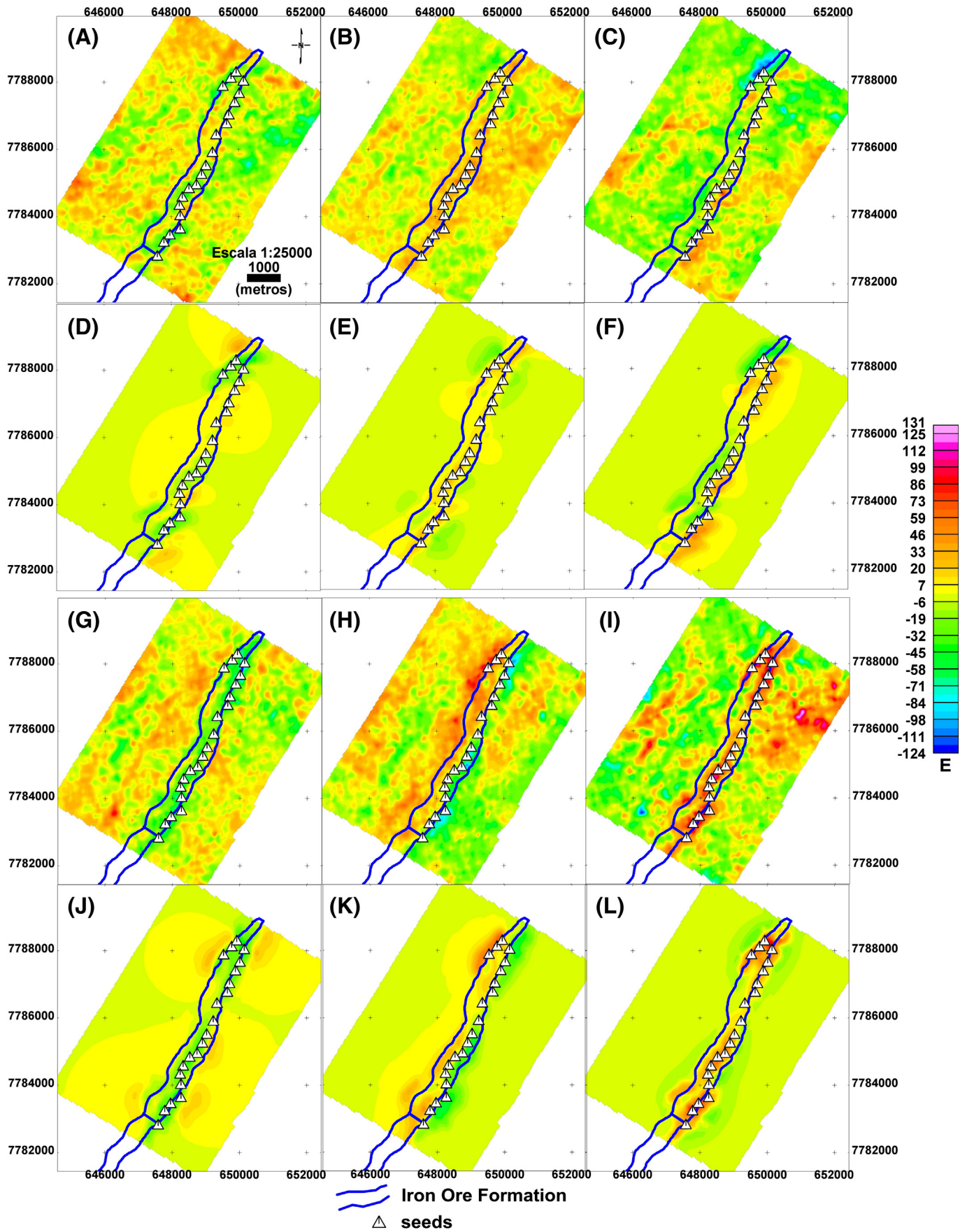
Fig. 8. Area 3. The observed (A–C and G–I panels) and predicted (D–F and J–L panels) g_{xx}-, g_{xy}-, g_{xz}-, g_{yy}, g_{yz}- and g_{zz}-components of the gravity gradient tensor. The latter were produced by the estimated density-contrast distribution shown in Fig. 9A. The white triangles represent the horizontal coordinates of the seeds used in the inversion. The blue lines delineate the mapped boundaries of the iron formation according to Dorr (1969). The location of Area 3 is shown in Fig. 5B. (For interpretation of the references to color in this figure legend, the reader is referred to the web version of this article.)

5. Results

First, we present a general view of the estimated iron-ore body obtained by using Uieda and Barbosa's (2012a) inversion. Next, we present a detailed view of the estimated iron-ore body and an integrated analysis of this estimate and the borehole data in order to validate the 3D geological model of the iron-ore formation over the southern flank of the Gandarela syncline.

5.1. General results

Fig. 9A displays a perspective view of the 3D estimated density-contrast distribution. This result confirms that the estimated iron-ore mineralization (pink volume) is shallow and has a northeast-elongated form. It is noteworthy that our estimate is segmented. This segmentation was not expected because, according to the geologic mapping presented by Dorr (1969), the iron-ore body within the Gandarela syncline would be continuous. The segmentation of the ore body cannot be verified through drill holes because the place where it occurs has difficult access. However, we argue that this result is reasonable because it seems to be controlled by a known northwest–southeast fault (not shown) which segmented the terrain close to this area.

By comparing Fig. 9A with the geological map (Fig. 9B) we can notice the strong correlation between our estimate of the iron-ore body and the outcropping iron-ore deposits of the Cauê Formation over the Gandarela syncline. Although the geological map does not show an outcrop in the transition between Areas 2 and 3, our estimate shows outcropping iron deposits. However, borehole information shows that, in this place, the iron-ore deposits are underlying a thin layer of duricrusts that are made up of high concentrations of iron oxides and iron hydroxides.

According to Fig. 3, the Fundão Fault controls part of the iron-ore deposit in the Gandarela syncline. However, this control does not occur in the study area, as is observed in the geological map (Fig. 9B). In fact, our estimated iron-ore body (Fig. 9A) confirms this assertion. Additionally, we also verify a southwestward increase in the width of the estimated iron-ore body, which is corroborated by the surface geology. This increase is probably controlled by the Gandarela syncline, whose role in this increase will be discussed later. Our estimated iron-ore body reveals a predominantly compact source with a variable depth to the bottom. The average estimated thickness of the iron-ore body is about 250 m.

The color-scaled maps (panels D–F and J–L) in Figs. 6–8 show the predicted data caused by the estimated density-contrast distribution shown in Fig. 9A. Notice that the inversion method used fits reasonably well with the data set over the elongated southwest–northeast feature which is mostly produced by the iron-ore deposit of the Cauê Formation (the targeted source) and allows large data residuals (the difference between the observed and predicted data) in other areas (non-targeted sources). We stress that this inversion method has the advantage of requiring no assumption about the density contrasts and the approximate depths of the nontargeted sources. Hence, Uieda and Barbosa's (2012a) method does not require data preprocessing to remove the gravity-gradient signals produced by the nontargeted sources, which makes it operationally simple.

5.2. Detailed results

We present a detailed analysis based on the integration of the borehole geology database and the estimated shape of the iron ore. We compare nine vertical cross-sections of the estimated density-contrast distribution (AA′–II′ in Fig. 9) to the available drill hole data. For this analysis, we superimpose on the cross-sections of the estimate of each lithologic logging data of a drill hole, whose horizontal coordinates coincide with a cross-section line. Drill-hole data close to a cross-section line of the estimate are projected onto the estimate.

Figs. 10–12 show the cross-sections of the estimate over Areas 1–3, respectively. Figs. 10A–12A show the predicted data (color scale map), cross-sections (white lines), seeds for the inversion (white triangles), and locations of the boreholes (yellow circles). The lithologic intervals from the drill holes are shown in color-scaled ribbons. One can expect that the estimated density contrasts of 0.75 g/cm^3 (pink areas) represent the iron-ore body. The targeted rocks for the iron formations consist of the soft, hard and semi-hard itabirites and hematites (shown in red, magenta and the shades of blue in the color-scaled ribbons); hence, we may expect the coincidence between pink areas in the estimate and these lithologies.

In cross-section AA′ (Fig. 10B), our estimated density-contrast distribution (pink area) indicates the existence of iron-ore masses in agreement with the targeted lithologies drilled by the boreholes a1, a2 and a3. Notice that our estimate shows that the iron-ore deposit does not extend to the south. Rather, it indicates the presence of iron ore at the northernmost portion of the cross-section which could be confirmed if a new borehole were drilled.

In cross-section BB′ (Fig. 10C), our estimated density-contrast distribution (pink area) is also consistent with the targeted litholo-gies (magenta and the shades of blue) from the boreholes b1, b2 and b3. Boreholes b1 and b3 drilled through a sequence of layers of hard, soft and semi-hard itabirites. Only the borehole b2 drilled through a sequence of layers of both soft to hard itabirite and soft hematite. In agreement with the northernmost portion of the cross-section AA′ (Fig. 10B), the estimate along the cross-section BB′ shows that the iron-ore deposit extends to the northwest portion of the cross-section.

In cross-section CC′ (Fig. 10D), our estimated density-contrast distribution (pink area) is in good agreement with borehole c1, which is mostly composed of soft, hard and semi-hard itabirites and soft hema-tites. Borehole c2 was drilled deeper to 450 m, going through a thick sequence of soft and goethitic hematites and alternate thick layers of soft and semi-hard itabirites (the shades of blue in the color-scaled ribbons). However, our estimate retrieves a thinner mass of iron ore only 225 m thick. On the other hand, close to borehole c3 we can see that our estimate does not predict iron ore in the subsurface. This agrees reasonably well with borehole c3, which drilled through nontargeted rocks (a duricrust layer).

The most striking feature of cross-sections AA′, BB′, CC′ is that they are over a duricrust, as shown in Fig. 9B. However, it is noteworthy that both our estimate and the boreholes find the iron ore in the subsurface.

In Fig. 11B, borehole d1 drilled a near-surface duricrust layer and a thick layer of soft itabirite. This borehole coincides with the vertical cross-section DD′, in which we can see that our estimate agrees reasonably well with the information from borehole d1. Besides, our estimate indicates the existence of iron-ore masses extending to the northwest direction.

Fig. 11C displays cross-section EE′ which coincides with two bore-holes, e1 and e2. Both boreholes drilled through a sequence of layers of itabirite and hematite, which mostly comprises soft and semi-hard itabirites and soft and hard hematites. For this cross-section, we estimate a maximum iron-ore thickness of 300 m. However, around borehole e2 our estimate (pink area) only indicates an approximately 125 m thick iron ore, while the borehole encountered an up to 325 m thick layer of iron ore.

Fig. 11D shows that the estimated iron-ore mass (pink area) along the vertical cross-section FF′ is shallower and extends to the southeast, similar to cross-section GG′ in the neighboring Area 3 as shown below. In this section FF′, our estimate agrees reasonably well with the information from borehole f2 which drilled layers of soft itabirite. However, our estimate fails in retrieving any mass of iron ore around borehole f1, which drilled through only a thin layer of soft hematite.
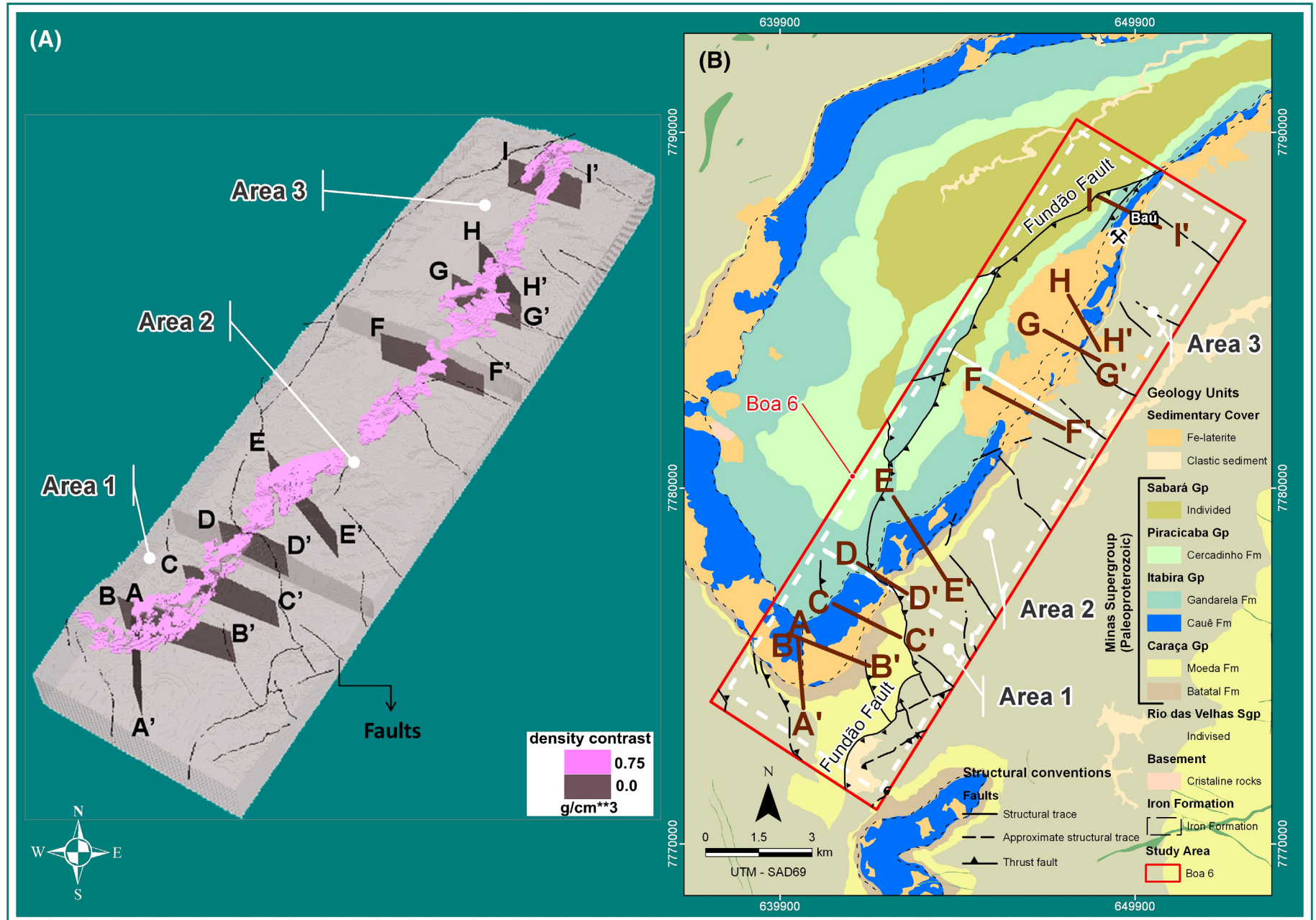
Fig. 9. (A) Tridimensional view of the estimated density-contrast distribution (in pink) with density contrast 0.75 g/cm^3, corresponding to the iron-ore body of the Cauê Formation. This estimate is obtained by inverting the gravity-gradient data sets from Areas 1–3 shown in Figs. 6–8 (color-scaled maps in panels A–C and G–I). (B) Geologic map of the study area showing Areas 1–3 which were used by applying Uieda and Barbosa's (2012a) method. The brown lines AA'–II' display the locations of the vertical cross sections described in Figs. 10–12. (For interpretation of the references to color in this figure legend, the reader is referred to the web version of this article.)
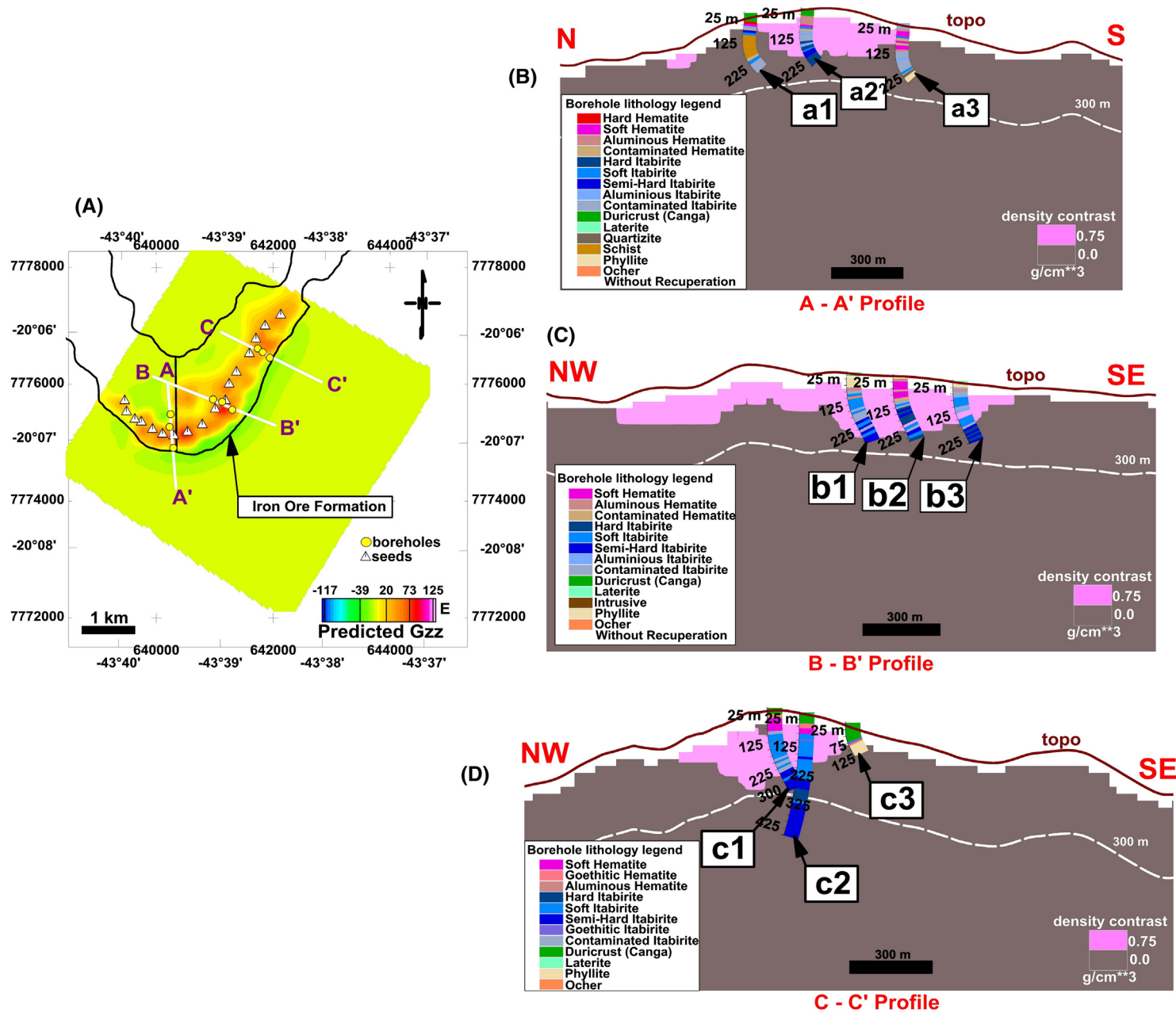
Fig. 10. Area 1. (A) The predicted g_{zz}-component of the gravity gradient tensor. The white lines AA′, BB′, and CC′ display the locations of the vertical cross sections described in (B), (C) and (D), respectively. The yellow dots and the white triangles show the horizontal coordinates of, respectively, the boreholes and the seeds used in the inversion. (B), (C), and (D) show vertical cross sections along profiles AA′, BB′ and CC′, respectively, displaying the estimated density-contrast distribution (in pink) with density contrast 0.75 g/cm³. The color ribbons in (B)–(D) represent the lithological intervals intersected by boreholes (a1–a3, b1–b3, c1–c3). (For interpretation of the references to color in this figure legend, the reader is referred to the web version of this article.)
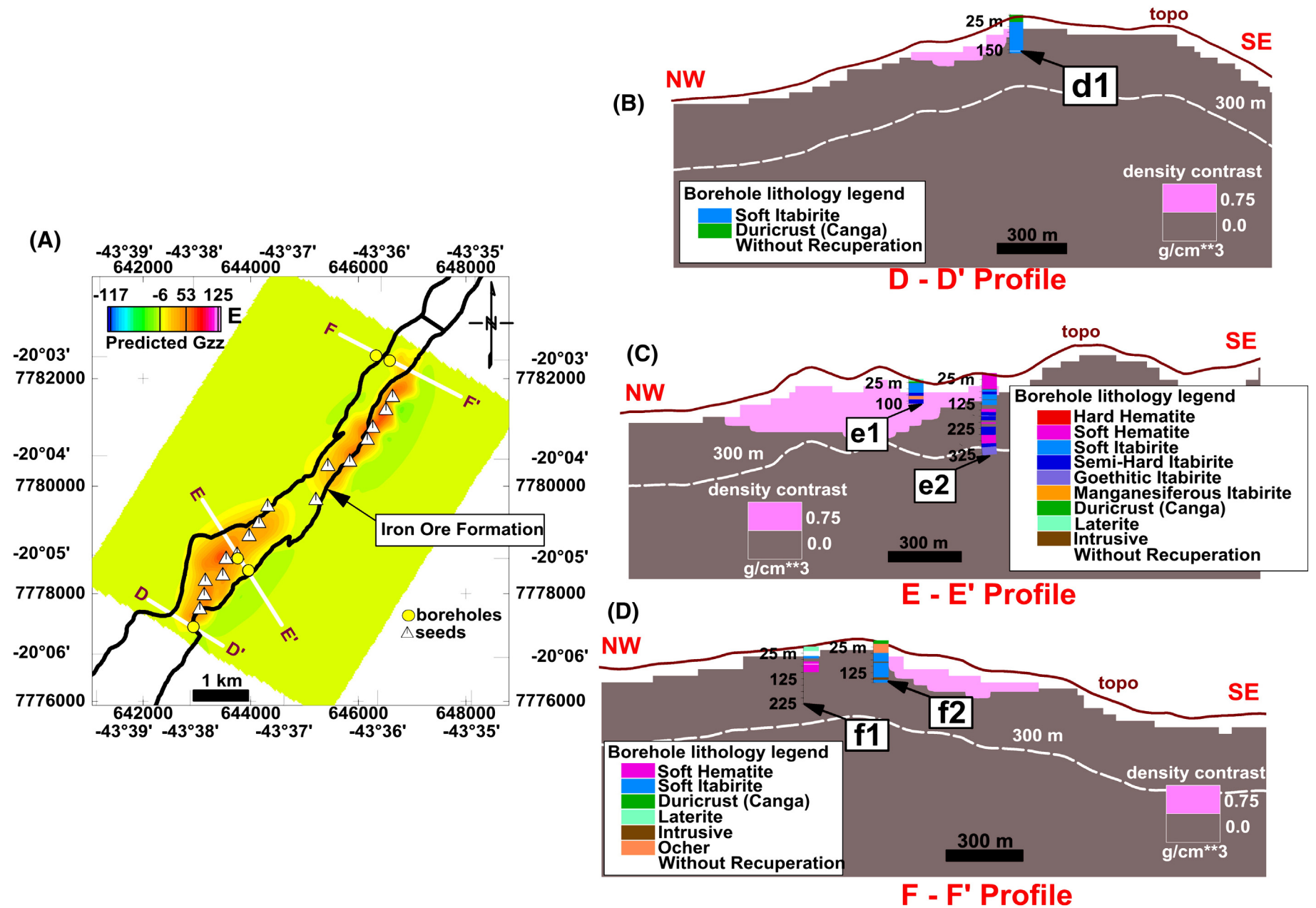
Fig. 11. Area 2. (A) The predicted g_{zz}-component of the gravity gradient tensor. The white lines DD′, EE′, and FF′ display the locations of the vertical cross sections described in (B), (C) and (D), respectively. The yellow dots and the white triangles show the horizontal coordinates of, respectively, the boreholes and the seeds used in the inversion. (B), (C), and (D) show vertical cross sections along profiles DD′, EE′, and FF′, respectively, displaying the estimated density-contrast distribution (in pink) with density contrast 0.75 g/cm³. The color ribbons in (B)–(D) represent the lithological intervals intersected by boreholes (d1, e1, e2, f1 and f2). (For interpretation of the references to color in this figure legend, the reader is referred to the web version of this article.)
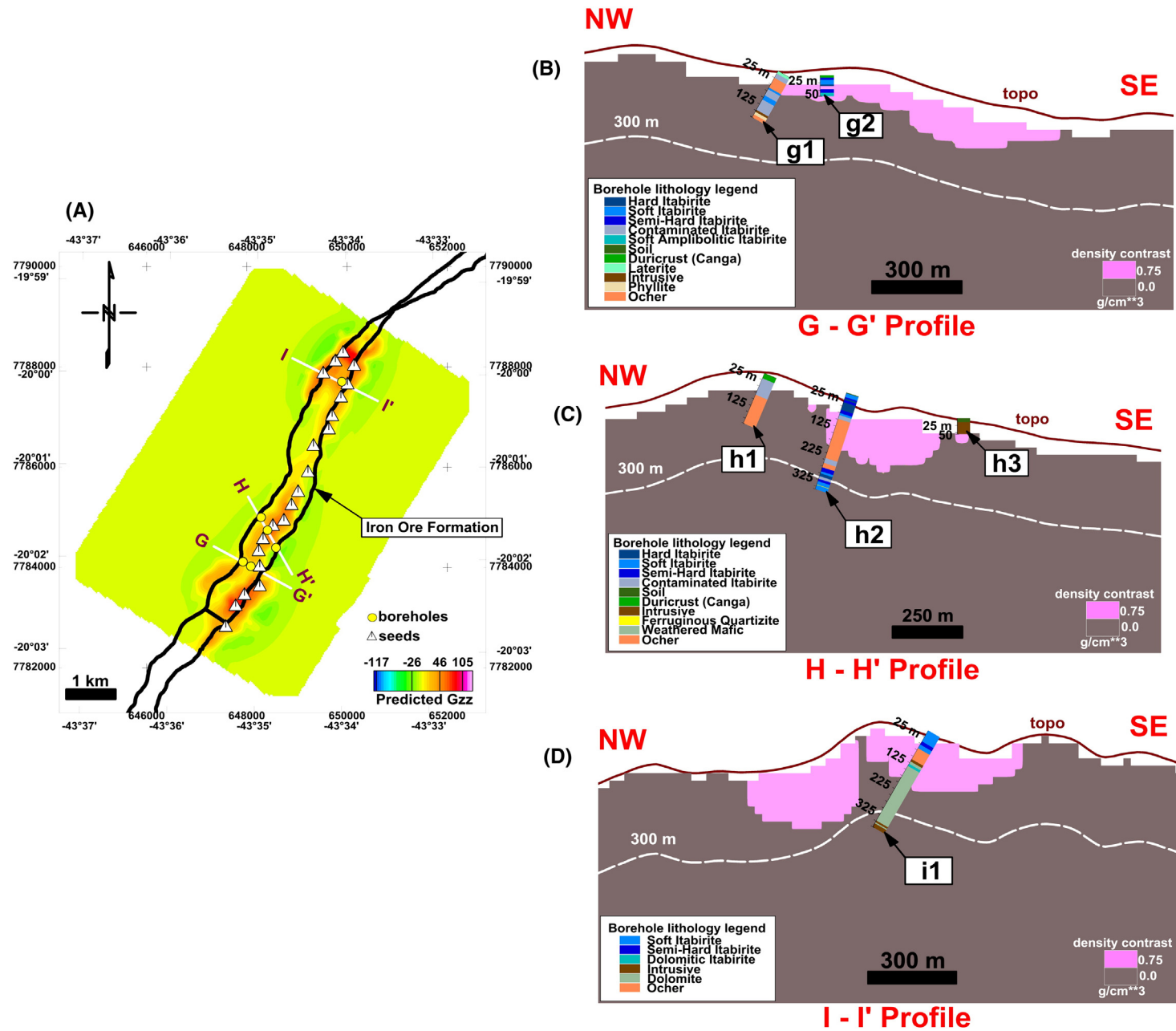
Fig. 12. Area 3. (A) The predicted g$_{zz}$-component of the gravity gradient tensor. The white lines GG′, HH′, and II′ display the locations of the vertical cross sections described in (B), (C) and (D), respectively. The yellow dots and the white triangles show the horizontal coordinates of, respectively, the boreholes and the seeds used in the inversion. (B), (C), and (D) show vertical cross sections along profiles GG′, HH′, and II′, respectively, displaying the estimated density-contrast distribution (in pink) with density contrast 0.75 g/cm³. The color ribbons in (B)–(D) represent the lithological intervals intersected by boreholes (g1, g2, h1–h3, and i1). (For interpretation of the references to color in this figure legend, the reader is referred to the web version of this article.)

Fig. 12B shows the vertical cross section GG′ which coincides with boreholes g1 and g2. Borehole g2 drilled through 75 m of soft, semi-hard and hard itabirites. These units make up most of the iron-ore formation in the Quadrilátero Ferrífero. In the proximity of this borehole, our maximum estimated depth to the ore bottom of about 80 m approximately coincides with the maximum depth attained by borehole g2. In contrast with borehole g2, which is dominated by targeted rocks for iron exploration, borehole g1 (Fig. 12B) drilled 37 m of ocher itabirite followed by 86 m of alternating thin layers of contaminated and soft itabirites. The ocher and contaminated itabirites are non-targeted sources for mineral exploration. Near borehole g1, we note that our estimate suggests a near surface iron mass. Hence, our result does not distinguish the thin layers of soft itabirite from the contaminated itabirite. This result is expected because of the inevitable loss of gravity-gradient data resolution with depth. Up to date, no inversion method can recover multiple and deep thin iron-ore layers.

The transition between Areas 2 and 3 deserves special attention. In Area 3, our estimate shows that the iron-ore mineralization does not extend to the northwest. Rather, it extends to the southeast. This southeastern extension along cross-section GG′ (Fig. 12B), located in the Area 3, is in close agreement with the continuity of the iron-ore body to the neighboring Area 2 in cross-section FF′ (Fig. 11D). The lack of estimated iron-ore mass extending itself northwestwards is corroborated by borehole g1 (Fig. 12B), which does not drill thick masses of the iron formation.

Fig. 12C shows the vertical cross-section HH′ which coincides with three boreholes (h1–h3). This is an interesting cross-section because of the presence of two deep boreholes, h1 and h2. The footages of the boreholes are 175 m and 325 m, respectively. Borehole h1 is dominated by nontargeted rocks for iron exploration (duricrusts, contaminated itabirite and ocher itabirite). Notice that our estimate does not predict iron-ore mass around borehole h1, showing close agreement with the lithologic units drilled through the borehole. Borehole h2 drilled through two sequences of targeted rocks composed of intercalated layers of soft, hard and semi-hard itabirites separated by a large layer of ocher itabirite, a nontargeted rock which is a kind of itabirite but with a high grade of aluminum. The first sequence is shallow-bottomed layers of itabirites which attains a maximum bottom depth of 85 m. The second sequence is deep-bottomed layers of itabirites which is found over the depth interval of 275–325 m. As previously explained, the gravity-gradient data do not have enough resolution to resolve deep iron-ore masses. Hence, our estimate retrieves a near-surface mass of iron ore being consistent with the gravity-gradient data resolution. Close to borehole h3, our inversion estimates masses of iron ore at the surface (pink area in Fig. 12C); however borehole h3 drilled through intrusive (dense) rocks indicating that our result failed. This failure is due to the inevitable ambiguity of gravity and gravity-gradient data interpretation. The iron ore and intrusive rocks may have the same densities; hence, it is impossible to differentiate between them using only gravity data.

Notice that both profiles GG′ (Fig. 12B) and HH′ (Fig. 12C) lie mostly over a duricrust (Fig. 9B) which is a nontargeted source in the study area. However, both the estimated density-contrast distribution in the subsurface and the boreholes show that we can find targeted sources (iron ore) beneath the Earth along these profiles (Fig. 12B and C).

Fig. 12D shows the vertical cross section II′ which coincides with one borehole (i1) whose footage is greater than 350 m. This borehole drilled through a 75 m thick sequence of targeted rocks that are made up of soft and semi-hard itabirites followed by nontargeted rocks that are made up of ocher itabirite from a depth of 75 to 100 m, and a thick layer of dolomite and dolomitic itabirite from a depth of 100 m to 330 m. Our estimate (pink area in Fig. 12D) retrieved the shallow-bottomed layers of itabirites in agreement with the i1 borehole.

6. Discussion

In the previous section we validated most of our estimated shape of the iron-ore body (Fig. 9A) by using the lithologic logging data of drill holes. Our estimated iron-ore mass agrees reasonably well with the information provided from the boreholes. In our research, the estimated 3D geometry of the entire iron-ore mineralization confirms known geologic features such as the northeast strike and the southwestward increase in its width (Fig. 9A).

Martinez et al. (2013) performed an inversion using Li's (2001) method on the same data set. However, they only used a small area of the data which approximately coincides with Area 3. Nonetheless, their results show close agreement with our results for Area 3.

Our estimated iron-ore mass discloses some previously unknown features which deserve to be highlighted. These features of the iron-ore body are as follows:

- It is not a continuous single body. Rather, in the central part of the study area, it is segmented into two parts (Fig. 9A). The breakup of the iron-ore body may be related to the northwest-trending faults which are perpendicular to the northeast-trending axis of the Gandarela syncline.
- Its thickness is variable along its strike, as shown in Figs. 9, 10C, 11C and 12B.
- Its thickness increases southwestwards (Figs. 10D and 11B). This increase combined with the southwestward increase in width (Fig. 10C) leads to a southwestward increase in the volume of the iron deposit. To date, this increase in iron volume toward the southwest was unknown because part of the iron body is masked by overlying duricrust (Fig. 9B).
- It appears to have variable dip directions. In the central part of the study area, the estimated iron-ore body is not dipping (Fig. 11C). Conversely, in the southernmost limit of the study area the retrieved iron-ore masses are dipping in the inward direction of the Gandarela syncline axis (Fig. 10C). In the northernmost limit, the dip is in the outward direction (Fig. 12B).

The larger volume of the iron-ore mass in the southwest portion of the study area might be related to the structural framework of the Gandarela syncline. A thicker iron-ore body would be expected due to the hinge zone of the Gandarela syncline which corresponds to the zone of maximum compression.

Two noteworthy limitations of our results deserve discussion. The first limitation is related to the resolution of the gravity-gradient data. Our result is unable to resolve multiple thin iron-ore layers vertically separated from each other by non-iron rocks (e.g., ocher itabirite); instead a single and compact iron-ore mass is estimated such as shown in Fig. 12B and C (pink area). The second limitation is due to the inherent ambiguity of gravity-gradient data interpretation. Our result does not distinguish between iron-ore mineralization and intrusive rocks because they have approximately the same density (Fig. 12C).

We stress that our estimated iron-ore mass agrees reasonably well with the information provided from the boreholes. Notwithstanding this agreement, we recall that the inversion of the gravity-gradient data was accomplished after the drill holes have been drilled. We call to attention that if the inversion approach had been performed at the early stages of the exploration program, before the drilling program, the estimated iron-ore mass could be used to guide the geologists in the drill planning. As a consequence, the number of drilled boreholes could be reduced and more suitable locations of the boreholes could be chosen.

Our geophysical study presents the advantage of allowing not only the visual representation of the 3D geometry of the iron-ore body but also an assessment of the iron-ore reserves. By using the estimated shape of the iron-ore body (Fig. 9A), we calculated an iron-ore volume

of about 965 million m^3. Assuming that the estimated density contrast of 0.75 g/cm^3 is due to the presence of hard itabirite only, whose density is 3.11 g/cm^3, the estimated iron-ore mass (not to be confused with the anomalous mass) is approximately 3 billion metric tons.

7. Conclusions

We used the method named "3D inversion by planting anomalous densities" for estimating the geometry of the iron-ore deposit over the southern flank of the Gandarela syncline within the Quadrilátero Ferrífero in southeastern Brazil. By jointly inverting all airborne gravity-gradient tensor components, we estimated a 3D density-contrast distribution that approximately mapped the shape of the targeted iron-ore bodies of the study area. Our result produced a voxel image of the 3D density-contrast distribution corresponding to the iron-ore body of the Cauê Formation composed of itabirites. Because of the computational efficiency of the inversion method employed, we were able to use a fine mesh comprising about 8.5 million prisms and all 91 thousand gravity-gradient observations.

The previous geologic mapping of this study area delineated the boundaries of the iron mineralization in plan view. However, part of this mapping was inferred by the geologists because most of the iron mineralization is masked by overlying duricrusts. Hence, the detailed 3D shape of the iron-ore body and its spatial distribution were not known either on the surface or in the subsurface.

Our estimate of the iron-ore shape is in agreement with the information provided by the lithologic logging data of drill holes. The estimated 3D shape of the iron-ore body confirms its northeast–southwest elongated form. This result also reveals that the iron-ore deposit is strongly controlled by the Gandarela syncline. The large estimated volume of the iron-ore mass seems to be controlled by the hinge zone of the syncline. The dip direction of the estimated iron ore seems to be variable. At the hinge zone of the Gandarela syncline the estimated iron body dips inwards towards the syncline axis. In the central portion of the study area, the estimated iron body seems not to be dipping, while in the northernmost portion it dips outwards from the syncline axis. In contrast with previous geological mapping, our result suggests a discontinuous iron-ore body. The breakup of the iron-ore body in the central part of the study area may be related to the northwest-trending faults which are perpendicular to the northeast-trending axis of the Gandarela syncline.

Our work allows not only the assessment of the 3D geometry of iron-ore body over the southern flank of Gandarela syncline, but also the estimate of the iron-ore reserve, which is about 3 billion tons. This result can be used in the mine planning strategy.

Acknowledgments

References

Alkmim, F.F., Marshak, S., 1998. Transamazonian orogeny in the Southern Sao Francisco Craton Region, Minas Gerais, Brazil: evidence for Paleoproterozoic collision and collapse in the Quadrilátero Ferrífero. Precambrian Res. 90, 29–58.

Alkmim, F.F., Martins-Neto, M.A., 2012. Proterozoic first-order sedimentary sequences of the São Francisco craton, eastern Brazil. Mar. Pet. Geol. 33, 127–139.

Bell Geospace, 2010. Processing and acquisition of air-FTG data and airborne magnetics. Trill Project and Extension — Sudbury Basin, Ontario, Canada (55 pp.).

Braga, M.A.S., 2009. Aplicação de Aerogradiometria Gravimétrica 3D-FTG na Prospecção de Minério de Ferro no Quadrilátero Ferrífero (MG) e Modelagem 2D e 3D para Estimativa de Massa do Depósito de Ferro de N1 em Carajás (PA). (Tese de Doutorado) Universidade Federal do Rio de Janeiro (271 pp.).

Chemale Jr., F., Rosière, C.A., Endo, I., 1994. The tectonic evolution of the Quadrilátero Ferrífero, Minas Gerais, Brazil. Precambrian Res. 65, 25–54.

Dorr, J.V.N., 1965. Nature and origin of the high-grade hematite ores of Minas Gerais, Brazil. Econ. Geol. 60 (1), 1–46.

Dorr, J.V.N., 1969. Physiographic, stratigraphic and structural development of the Quadrilátero Ferrífero, Minas Gerais, Brazil. U.S. Geol. Surv. Prof. Pap. 641-A, 1–110.

Gasparini, P., Mantovani, M.S.M., Corrado, G., Rapolla, A., 1979. Depth of Curie temperature in continental shields: a compositional boundary? Nature 278, 845–846.

Herz, N., 1970. Gneissic and igneous rocks of the Quadrilátero Ferrífero, Minas Gerais, Brazil. U.S. Geol. Surv. Prof. Pap. 641 (B) (58 pp.).

Huang, H., 2008. Airborne geophysical data leveling based on line-to-line correlations. Geophysics 73 (3), F83–F89.

Li, Y., 2001. 3-D inversion of gravity gradiometer data. 71st Annual International Meeting, SEG, Expanded Abstracts, pp. 1470–1473.

Lobato, L.M., Baltazar, O.F., Reis, L.B., Achtschin, A.B., Baars, F.J., Timbó, M.A., Berni, G.V., Mendonça, B.R.V., Ferreira, D.V., 2005. Projeto Geologia do Quadrilátero Ferrífero Integração e Correção Cartográfica em SIG com Nota Explicativa. CODEMIG. DVD, Belo Horizonte.

Martinez, C., Li, Y., Krahenbuhl, R., Braga, M.A., 2013. 3D inversion of airborne gravity gradiometry data in mineral exploration: a case study in the Quadrilátero Ferrífero, Brazil. Geophysics 78 (1), B1–B11.

Padilha, A.L., 1982. Implementação da Metodologia para Interpretação Magnética e sua Aplicação aos dados do Quadrilátero Ferrífero (MG). (Dissertação de Mestrado) Instituto de Astronomia e Geofísica, Universidade de São Paulo, Brazil (147 pp.).

Parasnis, D.S., 1966. Mining geophysics. Methods in Geochemistry and Geophysics. 3. Elsevier, Amsterdam (356 pp.).

Rolim, S.B.A., 2001. Resposta Geofísica dos Depósitos de Ouro da Porção Central do Quadrilátero Ferrífero. (MG. Tese de Doutorado) Instituto de Geociências, Universidade Estadual de Campinas (290 pp.).

Rosière, C.A., Rios, F.J., 2004. The origin of hematite in high-grade iron ores based in infrared microscopy and fluid inclusion studies: the example of the Conceição Deposit, Quadrilátero Ferrífero, Brazil. Econ. Geol. 99 (3), 611–624.

Silva, A.M., 1999. Integração de dados geológicos e geofísicos utilizando-se uma nova técnica estatística para seleção de alvos para exploração mineral, aplicada ao Greenstone Belt Rio das Velhas, Quadrilátero Ferrífero. (Tese de Doutorado) Universidade de Brasília (195 pp.).

Tavares, P., 1998. Identificação de Áreas Potencialmente Favoráveis a Mineralização Aurífera, a partir de Dados Estruturais e Aerogeofísicos aplicados a Terrenos do tipo "Greenstone Belt": O Caso da Folha Caeté, QF, MG. (Tese de Doutorado) Departamento de Geologia, Escola de Minas da Universidade Federal de Ouro Preto, MG (209 pp.).

Uieda, L, Barbosa, V.C.F., 2012a. Robust 3D gravity gradient inversion by planting anomalous densities. Geophysics 77 (4), G55–G66.

Uieda, L, Barbosa, V.C.F., 2012b. Animation of Growth Iterations during 3D Gravity Gradient Inversion by Planting Anomalous Densities. Figshare. http://dx.doi.org/10.6084/m9.figshare.91469.

Uieda, L, Barbosa, V.C.F., 2012c. Use of the "shape-of-anomaly" data misfit in 3D inversion by planting anomalous densities. SEG Technical Program Expanded Abstracts, pp. 1–6.

Villaça, J.N., Moura, L.A.M., 1981. Uranium in the Precambrian Moeda Formation, Minas Gerais, Brazil. U.S. Geol. Surv. Prof. Pap. 1161-T, T1–T14.